ACS APPLIED MATERIALS & INTERFACES

Research Article

www.acsami.org

Proton-Insertion-Enhanced Pseudocapacitance Based on the Assembly Structure of Tungsten Oxide

Minshen Zhu,[†] Wenjun Meng,[†] Yan Huang,[†] Yang Huang,[†] and Chunyi Zhi*[,†,‡]

[†]Department of Physics and Materials Science, City University of Hong Kong, 83 Tat Chee Avenue, Kowloon, Hong Kong

[‡]Shenzhen Research Institute, City University of Hong Kong, Shenzhen, P. R. China

Supporting Information

ABSTRACT: The capacitances of supercapacitors with carbon and metal oxides as electrodes are usually associated with the available surface areas of the electrode materials. However, in this paper, we report that proton insertion, an unusual capacitive mechanism, may effectively enhance the capacitance of metal oxides with low surface area but specific structures. Tungsten trioxide (WO_3) as the electrode material for supercapacitors has always suffered from low capacitance. Nevertheless, enhanced by the proton insertion mechanism, we demonstrate that electrodes fabricated by an assembly structure of hexagonal-phase WO_3 (h-WO_3) nanopillars achieve a high capacitance of up to 421.8 F g^{-1} under the current density of 0.5 A g^{-1}, which is the highest capacitance achieved with pure WO_3 as the electrodes so far, to the best of our knowledge. Detailed analyses indicate that proton insertion dominates the electrochemical behavior of h-WO_3 and plays the key role in reaching high capacitance by excluding other mechanisms. In addition, a thorough investigation on the temperature-dependent electrochemical performance reveals excellent performance stability at different temperatures. This study provides a new approach to achieving high capacitance by effective proton insertion into ordered tunnels in crystallized metal oxides, which is primarily important for the fabrication of compact high-performance energy storage devices.

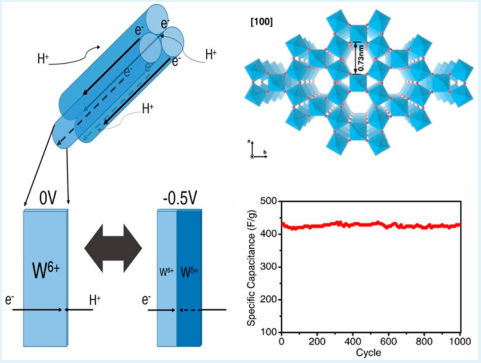

KEYWORDS: *insertion mechanism, tungsten oxide, supercapacitors, temperature-dependent performance*

1. INTRODUCTION

Regarding the increasing consumption of fossil fuels and continuous worsening climate, renewable energy resources, as well as clean energy devices, have started to take place in our daily lives. In the meantime, energy storage systems with high power density and/or high energy density have become more and more desirable.[1,2] Thereby, lithium-ion batteries[3−5] and electrochemical capacitors[6−15] are regarded as the most promising strategies for energy storage. Electrochemical capacitors, also known as supercapacitors, are the proposed energy storage systems for clean energy devices (e.g., hybrid vehicles, electric vehicles, etc.) and renewable energy generation facilities (e.g., wind power plant) benefiting from their excellent characteristics: long cycle life, superior power density, and high charging and discharging rates.[1,2,16] Moreover, with the concept of flexible and wearable devices becoming more and more popular, the convenience of the fabrication of solid-state and cable/wire-based supercapacitors drives the research on supercapacitors.[17−27] On the basis of the charge storage mechanism, supercapacitors can be divided into two categories: electric double-layer capacitors (EDLCs) and pseudocapacitors. For EDLCs, the charging mechanism is associated with the absorption and desorption of charge carriers at the electrode and electrolyte interfaces. However, pseudocapacitors utilize fast and reversible surface redox reactions so that they usually show much higher specific capacitances and energy densities than EDLCs.[16] For both mechanisms of charge storage, the amount of charge that can be stored is directly related to the amount of active material that can be easily accessed, which are usually materials on the surfaces. Accordingly, materials with large surface area, such as porous materials, are desired for application. Thereby, the synthesis of materials with large surface area attracts great research attention.

However, a detailed mechanism analysis indicates that pseudocapacitance can also come from the insertion of ions into precise pathways in the crystalline networks. The benefit of such pseudocapacitance is that large capacitance can still be achieved in a short period. Moreover, such a mechanism is still a capacitive process, which means that it will not be limited by slow solid-state diffusion.[28] This special pseudocapacitive mechanism sheds light on a new approach to producing better supercapacitors by using crystallized materials without porous structures. However, pseudocapacitors with high capacitances based on this mechanism are rarely reported.

Tungsten oxides are great electrochemically active materials for energy storage.[4,5,7,29−32] They have intriguingly fast and reversible surface redox reactions, which is associated with the

Received: July 21, 2014
Accepted: October 3, 2014
Published: October 3, 2014

similar W−O bond lengths in tungsten oxides with different oxidation states.[33] Furthermore, the intrinsic high densities of tungsten oxides show potential applications in the fabrication of compact devices with excellent power performance.[34] Theoretically, tungsten oxides are formed by corner and edge sharing of the WO_6 octahedra. By ordered stacking of WO_6 octahedra, a considerable number of interstitial sites can be formed. Such interstitial sites are effective accommodations for guest ions, rendering the absorption and desorption of ions at the surface, as well as insertion and deinsertion into the inner parts.[33,35] Among the different crystal structures of various tungsten oxides, the hexagonal-phase tungsten trioxide (h-WO_3) would be the most desired one for pseudocapacitors because it provides larger hexagonal tunnels in addition to the typical tetragonal tunnels.[35−40] These precise tunnels may benefit the insertion of guest ions into the tunnels existing in the h-WO_3 crystal structure. As a result, a high capacitance is expected to be obtained with h-WO_3 as electrodes for supercapacitor applications. To our best knowledge, pseudocapacitors based on t-WO_3 and m-WO_3 have been thoroughly reported, while h-WO_3-based supercapacitors have been scarcely reported.

Here, we reported a facile hydrothermal method to synthesize a novel assembly structure of h-WO_3 nanopillars via deintercalation of sodium tungstate. Surprisingly, the unique well-aligned structures show great potential in using nonporous crystalline materials as high-performance supercapacitor electrode materials via the unusual insertion-based pseudocapacitive mechanisms. As a result, the as-prepared h-WO_3 nanopillars show a very high capacitance (421.8 F g^{-1} under the current density of 0.5 A g^{-1}), which is the highest value reached by tungsten oxide materials so far, to the best of our knowledge. The detailed mechanism and key factors to achieve such high capacitance are thoroughly analyzed, which clearly reveals that proton insertion into hexagonal tunnels in h-WO_3 dominates the pseudocapacitive behavior. Moreover, we carried out a thorough investigation on the temperature-dependent capacitance performance of the assembly structure of h-WO_3 nanopillars because pseudocapacitance is based on a dynamic process, which might be severely affected by temperature variation.[41−47] The results revealed great performance stability at different temperatures and after rapid temperature-variation shocks.

2. RESULTS AND DISCUSSION

2.1. Characterization of h-WO_3 Nanopillars. As aforementioned, h-WO_3 is more desirable than t-WO_3 and m-WO_3 for supercapacitors. However, h-WO_3 is a metastable phase,[34] which means that it experiences phase transformation during the formation of nuclei. Therefore, a capping reagent is necessary to stabilize the formed h-WO_3 structures.[28,47−56] Herein, NaCl, a thoroughly investigated capping reagent, was used. The results revealed that h-WO_3 was successfully fabricated. The formation process of h-WO_3 has been thoroughly investigated by Wang et al.,[55,56] and the detailed process is shown in Figure S1 in the Supporting Information (SI). The as-prepared sample was examined by X-ray diffraction (XRD), as shown in Figure 1. It is clear that the product exhibits a single h-WO_3 phase (JCPDS no. 75-2187, hexagonal, $P6/mmm$). In addition, the intensive peaks indicate a well-crystallized structure of the as-prepared sample. Moreover, it should be noted that the intensity of the (001) peak is relatively stronger than that of the standard patterns, suggesting that the

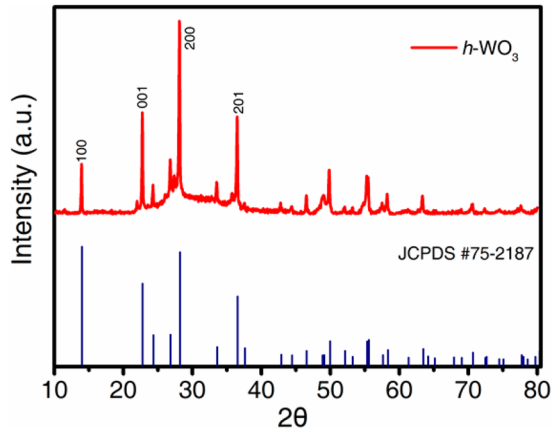

Figure 1. XRD pattern of as-synthesized h-WO_3.

h-WO_3 crystal may preferably grow along the [001] direction during the hydrothermal reaction.

The morphologies of the as-prepared materials were studied using scanning electron microscopy (SEM). As shown in Figure 2a, the as-prepared materials consist of h-WO_3 bundles with

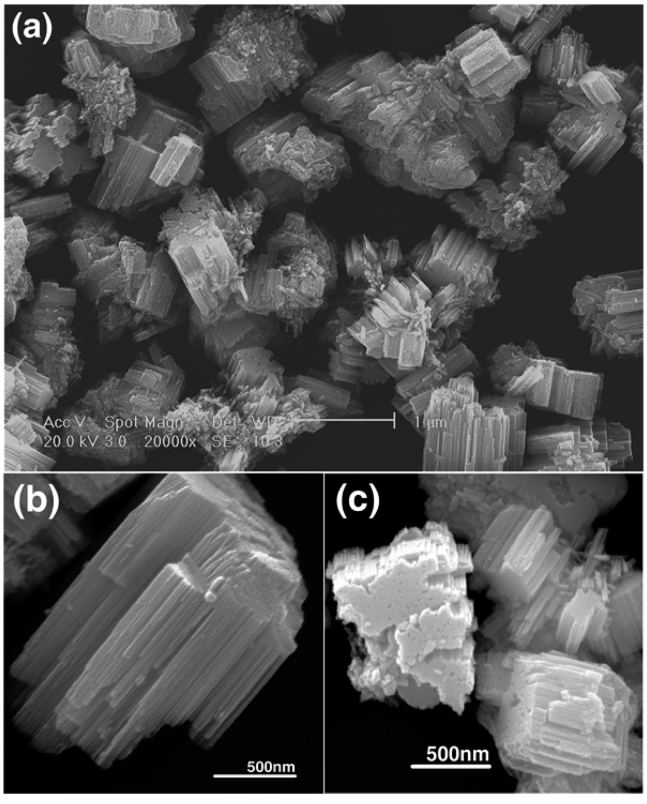

Figure 2. Low-magnification (a), high-magnification (b), and cross-sectional (c) SEM images of as-synthesized h-WO_3.

dimensions of submicrons. The magnified pictures shown in Figure 2b,c clearly reveal that h-WO_3 bundles are the assembly structure of aligned h-WO_3 nanopillars, which may result from the preferable [001] growth of h-WO_3. It should be noted that some pores are observed on the cross section of the bundles (Figure 3c), which may benefit penetration of the electrolyte.

Figure 3 displays transmission electron microscopy (TEM) and high-resolution TEM (HRTEM) images of the as-prepared assembly structure of h-WO_3 nanopillars. Figure 3a clearly

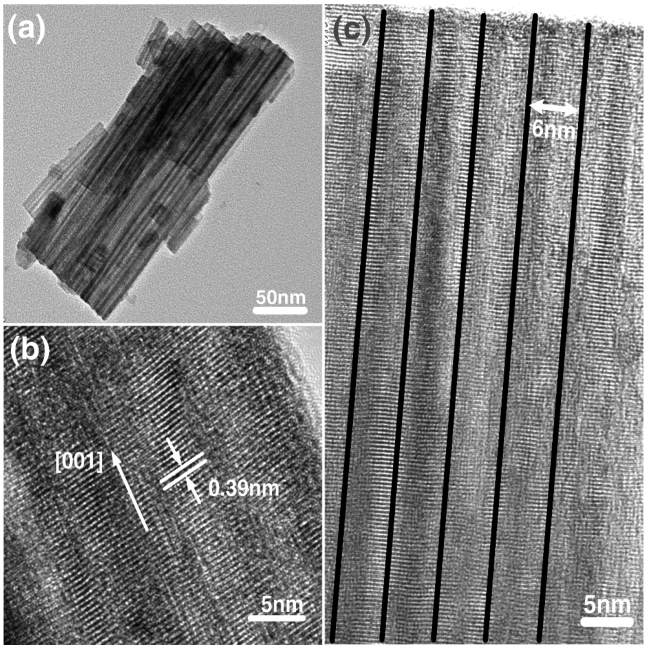

Figure 3. TEM (a) and HRTEM (b and c) images of the as-synthesized assembly structures of h-WO_3 nanopillars. The black lines show the boundaries of the pillars.

shows that an individual h-WO_3 bundle is assembled by highly aligned h-WO_3 nanopillars. The dimension of one single bundle is submicron, which coincides with the SEM observation shown in Figure 2. As shown in Figure 3b,c, the lattice spacing between adjacent planes is about 0.39 nm, which corresponds to the characteristic lattice spacing of the (001) planes of h-WO_3 (JCPDS no. 75-2187). This also indicates that the h-WO_3 nanopillars grow along the [001] direction, which confirms our assumption that the as-prepared h-WO_3 has a preferable [001] growth direction. This preferable [001] growth and the formation of nanopillar bundles are due to utilization of a capping reagent (NaCl), which can effectively suppress the growth of other lattice planes of h-WO_3, as demonstrated in Figure S1 in the SI. In addition, nanopillars with a diameter of about 6 nm can be evidently observed in Figure 3c. The smooth boundaries between the nanopillars may benefit the transfer of charges in electrochemical tests.

2.2. Electrochemical Characterization. In order to investigate the electrochemical performance of the synthesized materials, cyclic voltammetry (CV) was carried out within the potential range of −0.5 to 0 V versus a standard calomel electrode (SCE) in a three-electrode cell. Figure 4a shows the CV curves of the h-WO_3 electrodes with a scan rate of 2−20 mV s^{-1}. It is noted that CV curves at different scan rates present a near-rectangular and symmetric shape, while characteristic redox peaks can be observed at −0.2 and −0.34 V. This indicates a typical pseudocapacitive behavior and excellent reversibility. To achieve a profound understanding of the change of redox patterns, capacitance versus potential profiles, derived from dividing the measured current by the scan rate, are plotted in Figure 4b. At low scan rates, large anodic and cathodic peak capacitances can be clearly identified as 577.5 and 623.6 F g^{-1}, respectively. However, the shift of the anodic and cathodic peaks becomes much larger with increased scan rates, and distortion of the CV and capacitance patterns becomes more obvious as well, as shown in both parts a and b of Figure 4, which results from the finite time constant (τ), as shown in Figure S2 in the SI.

Capacitances of different scan rates can be calculated from the CV curves by using the following equation:

$$C_{CV} = \frac{1}{2mv\Delta V}\int I\,dV \qquad (1)$$

Here, m is the weight of the active material, v is the scan rate, ΔV is the potential range, and I is the current at certain potentials. The calculated capacitances at 2−20 mV s^{-1} are

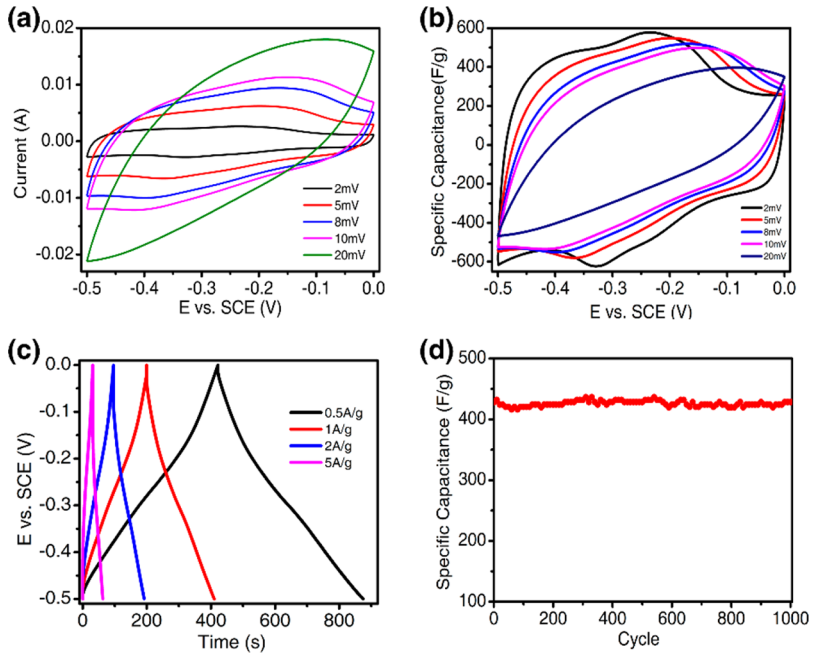

Figure 4. CV curves (a), profiles of capacitance versus potential (b), and charge−discharge profiles (c) measured at different rates and (d) cycling stability of the as-synthesized h-WO_3 nanopillars.

dx.doi.org/10.1021/am504756u | ACS Appl. Mater. Interfaces 2014, 6, 18901−18910

Table 1. Comparison of the Performances of Supercapacitors Based on Tungsten Oxides and Other Popular Active Materials

formula	specific capacitance	synthesis method	morphology	crystal structure	ref
h-WO_3	421 F g^{-1}	hydrothermal synthesis	aligned nanopillar bundles	hexagonal	this work
m-WO_{3-x}-C-s	103 F g^{-1}	block-polymer-assisted synthesis	hexagonal porous	triclinic	33
tOMC-$WO_{2.83}$	175 F g^{-1}	ordered mesoporous carbon-assisted synthesis	particles in mesoporous carbon	monoclinic	30
m-WO_3	199 F g^{-1}	template-assisted synthesis	mesoporous	cubic	31
WO_3–WO_3·0.5H_2O	293 F g^{-1}	microwave-assisted hydrothermal synthesis	disordered nanorods	hexagonal + cubic	28
a-WO_3	231 F cm^{-3}	microwave irradiaion	amophorous	amphorous	29
NiO	309 F g^{-1}	chemical bath deposition	nanosheets	cubic	11
$CuCo_2O_4$@MnO_2	296 F g^{-1}	hydrothermal synthesis	core–shell	cubic	21
Co_9S_8/Co_3O_4@RuO_2	4.28 F cm^{-3}	hydrothermal synthesis	nanorods@nanosheets		22
RuO_2·xH_2O	502 F g^{-1}	hydrolysis	hollow fusiform	amphorous	12
In_2O_3	64 F g^{-1}	filtration	nanowires		24
SnSe	1.8 mF cm^{-2}	sol–gel	nanowire	orthorhombic	25

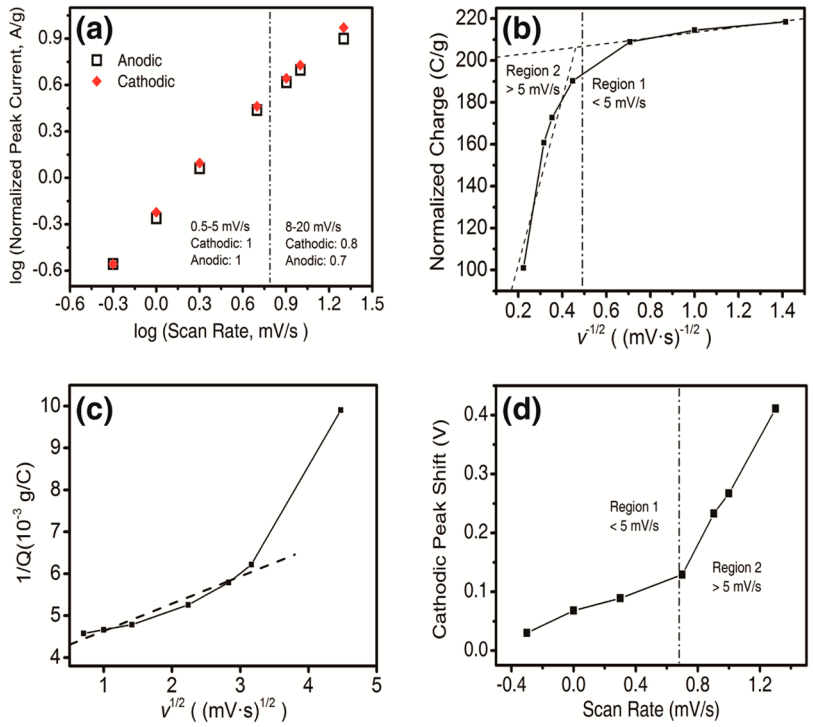

Figure 5. (a) b value determination of normalized anodic and cathodic peak currents, (b) plot of normalized charges versus $v^{-1/2}$, (c) plot of reciprocal normalized charges versus $v^{1/2}$, and (d) profile of the cathodic peak shift of as-synthesized h-WO_3.

417.8, 380.5, 345.5, 321.6, and 201.9 F g^{-1}, respectively. These large capacitances are confirmed by the capacitance obtained from galvanostatic charge–discharge profiles measured at 0.5–5 A g^{-1}, as shown in Figure 4c: the capacitance can reach 421.8 F g^{-1} at 0.5 A g^{-1} and maintain 311 F g^{-1} at a high charge–discharge rate (5 A g^{-1}). It should be noted that the high specific capacitance achieved here is quite impressive when compared with those of supercapacitors based on other tungsten oxide materials, and even other popular materials[11,12,21,22,24,25,28–31,33] (Table 1). In addition, the specific energy and power performance can reach near 10 Wh kg^{-1} at 1 kW kg^{-1} (Figure S3 in the SI). The results reveal a very competitive power performance compared with those of other materials, such as t-WO_3 (~0.02 Wh cm^{-3} at 1 W cm^{-3} with a density of 3.3 g cm^{-3}),[33] In_2O_3 (1.29 Wh kg^{-1} at 7.48 kW kg^{-1}),[25] NiO (~15 Wh kg^{-1} at 1 kW kg^{-1}).[12] The cycle ability is excellent, as shown in Figure 4d: almost 100% capacitance retention is achieved within 1000 cycles.

The high capacitance achieved is quite surprising considering the bulk features of the synthesized assembly structure of h-WO_3 nanopillars, which possesses a very small specific surface area of 26.4 m^2 g^{-1}, as revealed in Brunauer–Emmett–Teller analyses (Figure S4 in the SI). By common sense, a low surface area of the electrodes means that very limited active materials can contribute to the capacitance, which may eventually result in a low capacitance of the supercapacitor. Therefore, it is worth investigating the mechanism behind and uncover the unknown factors contributing to the large capacitance achieved in the assembly structure of h-WO_3 nanopillars.

2.3. Analyses of the Dominated Energy Storage Mechanism. It is well-known that electrochemical energy storage is dominated by two mechanisms: capacitive process and semiinfinite diffusion. Therefore, first, we will illustrate that energy storage by the assembly of h-WO_3 nanopillars is dominated by the capacitive process instead of semiinfinite

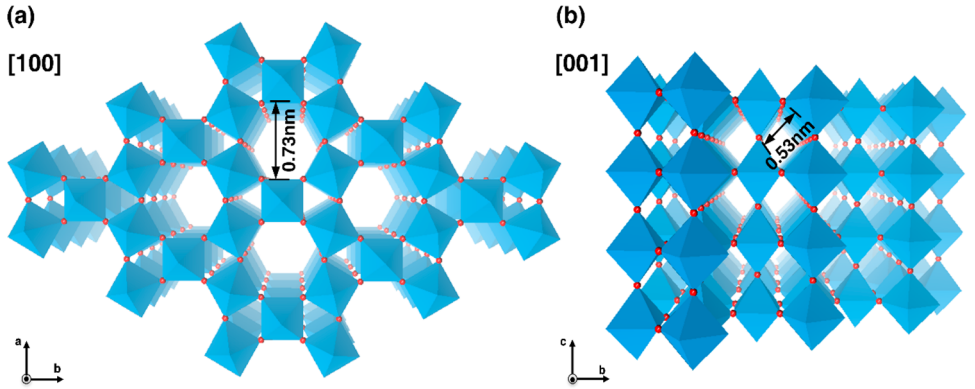

Figure 6. (a and b) Schemes of the hexagonal-phase tungsten oxides along the [001] and [100] directions of the microstructure of as-synthesized *h*-WO_3.

diffusion. As is known, the currents' changes in Figure 4a obey the power law:[57]

$$i = av^b \quad (2)$$

where i represents the current, v is the scan rate, and a and b are adjustable values. When the b value is 0.5, the current is controlled by semiinfinite diffusion, while a value of 1 indicates that the current is surface-dominated; that is, charge storage is a capacitive process. To probe the basic charge process behavior in the *h*-WO_3 electrodes, $\log(i)$ versus $\log(v)$ is plotted from 0.5 to 20 mV s^{-1} for both cathodic and anodic peaks, as shown in Figure 5a. Evidently, the b value (slope of the curve) is close to 1 for both cathodic and anodic peaks at scan rates ranging from 0.5 to 5 mV s^{-1}, indicating a surface-dominated kinetic, which reveals the capacitive behavior. Figure 5a also exhibits that the b value changes to 0.8 and 0.7 for cathodic and anodic peaks, respectively, when the scan rates are higher than 5 mV s^{-1}. This deviation may come from an increase of the ohmic contribution (resistance of the active material and its interface with the electrolyte) and diffusion limitations.

To further reveal the mechanism of the capacitance, the following calculations are carried out. According to the theory by Trasatti et al.,[58,59] the charges stored can be characterized by the dependence of voltammetric charges (Q) on the scan rates (v). The value of Q can be regarded as a sum of the charges resulting from capacitive behavior (Q_c) and the charges related to diffusion (Q_d):

$$Q = Q_c + Q_d \quad (3)$$

Assuming that semiinfinite diffusion is involved during the charge−discharge process, Q can be obtained by extrapolating the plots of Q versus $v^{-1/2}$ (Figure 5b). The linear region represents a limited diffusion process, whereas the capacitive behavior should be independent of the scan rates. Analogous to Figure 5a, the capacitive (region 1: <5 mV s^{-1}) and diffusion (region 2: >5 mV s^{-1}) regions can be divided in Figure 5b. With scan rates smaller than 5 mV s^{-1}, the value of Q is not very sensitive to variation of the scan rates. Thus, the extrapolated y intercept yields the capacitance that should solely originate from the capacitive behavior. The estimated charge is ~200.18 C g^{-1}, which is ~48% of the theoretical value calculated based on one-electron redox reaction with WO_3. However, in region 2 where the scan rates are higher than 5 mV s^{-1}, the diffusion process may limit the charging process; thus, the value of Q decreases near linearly with increasing scan rates. In addition, the charges associated with the most accessible areas, which are usually proportional to the specific surface area, can be estimated by extrapolation of the plot in region 2. The result shows that the capacitance coming from the most accessible area is only as low as ~23.23 C g^{-1}, which is in good agreement with the small specific surface area, as described before.

It is well-known that pseudocapacitance originates from three mechanisms: the underpotential deposition of metals, fast surface redox reactions, and ion insertion without phase changes.[3,4] Among these three mechanisms, the underpotential deposition and surface redox mechanisms are particularly associated with the specific surface area and exhibit the typical kinetics of the surface-controlled electrochemical process. However, the insertion-based pseudocapacitance is quite unusual. This is because most charge storage based on the insertion of ions into bulk materials is limited by the slow solid diffusion process, whereas the pseudocapacitive behavior needs a surface-controlled process just like the underpotential deposition and surface redox reactions.

According to the above analyses associated with Figure 5b, the capacitance related to the most accessible area is quite a small portion of the whole capacitance (23.23 C g^{-1} vs 23.23 + 200.18 C g^{-1}), and we can conclude that the high rate insertion of protons into the inner area of *h*-WO_3 nanopillars results in the high capacitance obtained. For further confirmation of the validity of this implication, the infinite-time charge is obtained by extrapolating the plot of $1/Q$ versus $v^{1/2}$ (Figure 5c). The result shows that the infinite-time charge is ~251.26 C g^{-1}, which is close to the result we estimated before (~200.18 C g^{-1}). On the basis of these analyses, we can confidently claim that the high capacitance obtained is associated with the high rate insertion of protons into tunnels in the *h*-WO_3 crystal lattice.

The other feature of the capacitive behavior of *h*-WO_3 at scan rates of <5 mV s^{-1} is that the peak potential shifts with the scan rates are relatively small. As exhibited in Figure 5d, the cathodic and anodic peak potential shifts are generally smaller than 0.1 V with scan rates below 5 mV s^{-1}. This is a good indication of the facile insertion of protons because the slow diffusion-controlled process will result in much larger peak shifts when the charge−discharge time is as short as 1 min such as in lithium-ion batteries.

The facile insertion of protons into *h*-WO_3 implies that the crystal structure offers precise transport pathways for protons. Parts a and b of Figure 6 show the (001) and (100) planes of *h*-WO_3. Evidently, the hexagonal crystal structure possesses a

large amount of tunnels: special hexagonal tunnels along the [001] direction (Figure 6a) and typical tetragonal tunnels formed by stacking of the WO_6 octahedra perpendicular to the [001] direction (Figure 6b). Obviously, the size and space of the hexagonal tunnels are almost 5 times those of the tetragonal tunnels because the area of the hexagonal tunnel is about 1.38 nm^2 while the area of the tetragonal tunnel is only about 0.28 nm^2. Consequently, the effective proton insertion depth of the hexagonal tunnels will be much longer than that of the tetragonal tunnels, resulting in a much higher proton insertion associated with capacitance. On the basis of these analyses, a huge amount of hexagonal tunnels contained in the as-synthesized assembly structure of *h*-WO_3 nanopillars would permit the exceptionally fast and precise insertion of protons. Meanwhile, the preferable [001] grown nanopillars enhance this effect, which is the key factor in achieving the very high capacitance. Additionally, detailed analyses on the capacitive behavior of *h*-WO_3 electrodes are elaborated in Figure S5 in the SI.

2.4. Electrochemical Impedance Spectroscopy (EIS) Tests. Furthermore, to gain insight into the capacitive behavior at different potentials, EIS tests were conducted. In Figure 7a,

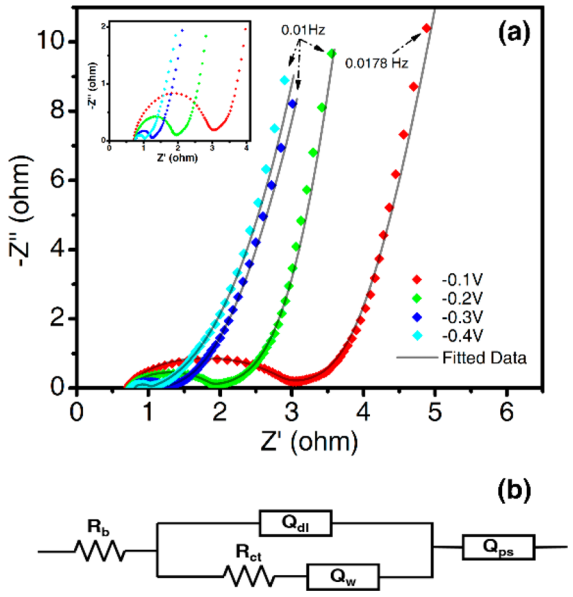

Figure 7. (a) Nyquist plots and best-fitted results and (b) equivalent circuit of the as-synthesized assembly structure of *h*-WO_3 nanopillars.

Nyquist plots at different potentials are shown in the frequency range of 100 kHz to 10 mHz. Typical impedance behaviors of pseudocapacitors are identified from the Nyquist spectra. The first intersection point with the real axis (represented by Z' in Figure 7a) in high-frequency region indicates the resistance of the electrolyte and intrinsic resistance of active materials (R_b). The semicircle in the high-frequency to midfrequency region was modeled by a charge-transfer resistance (R_{ct}) and the double-layer capacitance (Q_{dl}) connected in parallel. After the semicircle, the Nyquist plots show a tail in the low-frequency region with a change in the slope to vertical, which is correlated with the diffusion of protons into the active materials (Q_w). The following pseudocapacitance (Q_{ps}) is observed for nearly vertical rise. The electrochemical process observed from the Nyquist plots is represented by a modified Randles circuit with a set of resistors and constant phase elements (CPE, denoted as Q) in series and parallel, as shown in Figure 7b. The impedance of CPE can be expressed by the following equation:

$$\frac{1}{Z_{CPE}} = Y_{CPE} = Y_0(j\omega)^n \tag{4}$$

Here $\omega = 2\pi f$. For $n = 0$ and 1, CPE represents pure resistor and capacitor, respectively. Consequently, it is expected that the n value of Q_{dl} and Q_{ps} should be near 1. As mentioned before, diffusion would be involved in the charge−discharge process, whose impedance can be expressed by the following equation:

$$Z_w = \frac{A_0}{(j\omega)^n} \tag{5}$$

For the semiinfinite diffusion process, which is usually represented by Warburg diffusion, the n value will be 0.5.

By using the equivalent circuit shown in Figure 7b, Nyquist plots can be fitted, and the best-fitted results are displayed as a solid line in Figure 7a. Parameters of different elements in the equivalent circuit are shown in Table 2 ($\chi^2 < 10^{-3}$). As shown in Table 2, the value of R_b is around 0.8 Ω and remains invariant, while the charge-transfer resistance (R_{ct}) becomes much smaller at lower potential, indicating an easier transfer of charges. For a comparison of the capacitance, Q_{dl} is much smaller than Q_{ps}, suggesting that the capacitive behavior of the assembly structure of *h*-WO_3 nanopillars is mainly dominated by the pseudocapactive mechanism, whereas the n values of both Q_{dl} and Q_{ps} are near 1, as expected for the typical capacitive behavior. Furthermore, the values of Q_{dl} and Q_{ps} decrease with an increase of the potential, which is in good agreement with the results shown in Figure 5a,b. Meanwhile, deviation of the semiinfinite elements (Q_w) from the ideal semiinfinite diffusion (Warburg diffusion) becomes more severe at higher potential. This may be attributed to the exceptionally fast insertion of protons into *h*-WO_3, as analyzed before. Given the facile insertion of protons, it is reasonable to consider it to be a charge-transfer process, which may exhibit the behavior of the resistor. Thereby, the values of n at high potential are closer to 0 because at high potential the protons can insert into the inner part more easily with a small amount of inserted protons. This special phenomenon further confirms the insertion-enhanced capacitance of the as-synthesized assembly structure of *h*-WO_3 nanopillars.

Table 2. Parameters of Best-Fitted Results of EIS Spectra of the Assembly Structure of *h*-WO_3 Nanopillars

		Q_{dl}			Q_w		Q_{ps}	
V (V)	R_b (Ω)	Y_0 (F)	n	R_{ct} (Ω)	A_0 (Ω s^{-1})	n	Y_0 (F)	n
−0.1	0.74	1.6×10^{-4}	0.89	1.83	1.25	0.19	0.8336	0.96
−0.2	0.77	1.9×10^{-4}	0.90	0.98	0.88	0.26	1.685	0.99
−0.3	0.83	2.0×10^{-4}	1.00	0.35	0.70	0.35	1.992	0.97
−0.4	0.82	4.6×10^{-4}	1.00	0.19	0.81	0.42	2.13	1.00

2.5. Temperature-Dependent Performance of the *h*-WO_3 Electrodes. As we know, the temperature may severely affect the performance of supercapacitors, especially for pseudocapacitors. Herein we investigated the temperature effects on the *h*-WO_3 electrodes under various temperatures. At elevated temperature, the capacitance increases as indicated by charge−discharge profiles measured at 1 A g^{-1} (Figure 8a).

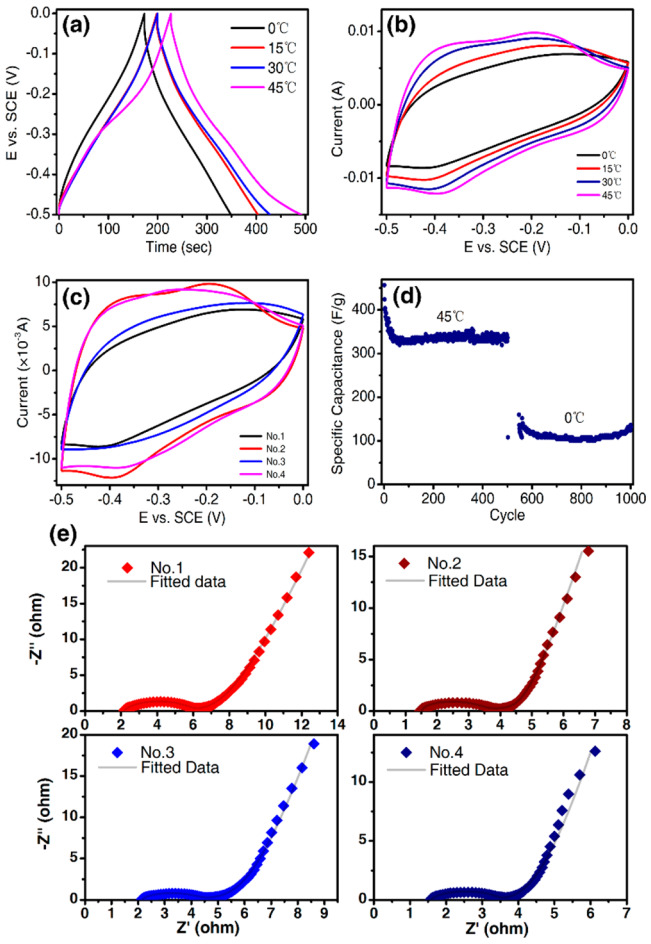

Figure 8. Electrochemical performances of *h*-WO_3 electrodes at different temperatures: (a) charge−discharge curves at different temperatures measured at 1 A g^{-1}; (b) CV curves at different temperatures measured at 8 mV s^{-1}; (c) CV curves under gentle and rapid temperature variation measured at 8 mV s^{-1}; (d) cycling performance under a rapid change of temperature; (e) Nyquist plots and fitted data under different conditions (nos. 1 and 3, 0 °C reached by gentle and rapid temperature variation, respectively; nos. 2 and 4, 45 °C reached by gentle and rapid temperature variation, respectively).

From 0 to 45 °C, a 31% increment is achieved from 346.4 to 453.6 F g^{-1}. This enlarged capacitance may be attributed to the enhanced mobility of ions in the electrolyte at elevated temperatures. Keep in mind that the crystal structure of *h*-WO_3 offers precise pathways for the insertion of protons. The improvement of the mobility of protons may lead to a more effective insertion based on the consideration that the relatively temperature change (0 to 45 °C) could not affect the structure of *h*-WO_3 (Figure S7 in the SI). Thereby, the capacitance would increase. This implication is testified by the EIS spectra shown in Figure S8 in the SI, where two intercepts of the real axis, representing the internal and charge-transfer resistance, become smaller at elevated temperatures, indicating a higher mobility of ions and an enhanced charge-transfer process. Moreover, the slope of the vertical line in the low-frequency region is larger, which indicates a more typical capacitive behavior. Besides, we conducted CV tests at a relatively high scan rate (8 mV s^{-1}) under different temperatures (0, 15, 30, and 45 °C). Analogous to the results of the charge−discharge profiles, the inner areas of the CV curves increase with elevated temperatures, indicating increases of the capacitances as well. The calculated capacitances at 0, 15, 30, and 45 °C are 241.8, 295.4, 350.2, and 386.4 F g^{-1}, respectively, which reveals a 60% increase. Besides, the detailed rate ability is shown in Figure S6 in the SI, which shows a very good rate ability at different temperatures.

In addition, sometimes supercapacitors may encounter the shock of temperatures, which may permanently result in the performance degradation of supercapacitors. To investigate the performance of *h*-WO_3 under such conditions, CV tests were carried out under a rapid change of temperature between 0 and 45 °C. The results of the CV tests are shown in Figure 8c. For a detailed comparison, the CV curves obtained at 0 and 45 °C by gentle temperature variation shown in Figure 8b are also shown in Figure 8c. Evidently, at the same temperature of either 0 or 45 °C, the capacitances after rapid temperature variation shocking are slightly larger. The high capacitance after temperature shocking from 45 to 0 °C can be attributed to the relatively high ion mobility that has not been stabilized at 0 °C in time. This high capacitance is temporary, and it will decrease quickly to a stable value with a few cycles, as revealed in Figure 8d.

However, compared with the capacitance at 45 °C reached through gentle temperature variation, the capacitance at 45 °C reached through rapid temperature variation is even higher, which is not expected and cannot be explained by considering the ion mobility of electrolytes. Moreover, it is also found that this discrepancy of capacitances is temporary and diminished in a few cycles (Figure 8d). To achieve a profound understanding of the reasons for such interesting results, EIS tests were conducted at the open-circuit potential at different conditions

Table 3. Parameters of the Best-Fitted Results of EIS Spectra under Different Conditions

		Q_{dl}			Q_w		Q_{ps}	
no.[a]	R_b (Ω)	Y_0 (F)	n	R_{ct} (Ω)	A_0 (Ω s^{-1})	n	Y_0 (F)	n
1	2.16	2.23×10^{-4}	0.79	3.48	2.13	0.24	0.60	0.91
2	2.13	2.27×10^{-4}	0.80	1.94	1.75	0.21	0.76	0.95
3	1.52	0.56×10^{-4}	1.00	1.03×10^{-7}	3.13	0.06	0.74	0.94
4	1.56	3.94×10^{-4}	0.82	1.78	1.20	0.96	0.94	0.28

[a]Nos. 1 and 2: 0 °C reached by gentle and rapid temperature variation, respectively. Nos. 3 and 4: 45 °C reached by gentle and rapid temperature variation, respectively.

(Figure 8e). The best-fitted results are listed in Table 3, which are obtained by using the equivalent circuit, as shown in Figure 7b. As aforementioned, the increase of the capacitance after temperature shocking from 45 to 0 °C is the result of temporary high ion mobility after a fast cooling process. Also, this claim is verified by a decrease of the charge-transfer resistance (R_{ct}, decrease from 3.48 to 1.94 Ω) and diffusion resistance (A_0, decrease from 2.13 to 1.75 Ω s^{-1}) after a fast cooling process. Meanwhile, the other parameters are quite close, indicating that the same capacitive behaviors are preserved. However, the parameters at 45 °C by a quick heating process are quite abnormal, especially for the charge-transfer resistance (R_{ct}), diffusion element (Q_w), and proposed pesudocapacitive element (Q_{ps}). Accordingly, it can be deduced that the capacitive behavior is severely affected by the rapid temperature variation shocking. The increase of the double-layer capacitive element and charge-transfer resistance can be explained by the near-surface insertion of protons. Such an insertion may directly contribute to the capacitance as the proposed diffusion element (Q_w) change to the capacitive element, which is implied by the n value (n = 0.96) as well. In addition, the change of the proposed pseudocapacitive value (n = 0.28) indicates the current leakage of the supercapacitor, which comes from the self-discharge phenomenon as a result of variation of the temperature. Such a self-discharging process may continuously suppress the capacitance of h-WO_3 electrodes until the performance becomes stable, as revealed in Figure 8e.

3. CONCLUSION

In conclusion, proton insertion, as an unusual mechanism for electrochemical storage, is found to dominate the capacitive behavior of a crystalline assembly structure of h-WO_3 nanopillars and provides remarkably enhanced capacitance. Detailed analyses indicate that the intrinsic multitunnel structure of the fabricated h-WO_3 assembly is the key factor to achieving the effective insertion of protons. Consequently, the as-prepared h-WO_3 nanopillar assembly exhibits a very high electrochemical capacitance of 421.8 F g^{-1} under the current density of 0.5 A g^{-1}, which is the highest capacitance achieved so far for tungsten oxide materials, to the best of our knowledge. Subsequently, a comprehensive investigation on the temperature-dependent capacitance performance revealed a great performance stability of h-WO_3 nanopillar electrodes at different temperatures. Our studies demonstrate that non-porous electrode materials can still achieve high capacitance through the proton-insertion mechanism, which may pave a novel way for the fabrication of electrochemical energy storage with high performance. In addition, as a multifunctional material, the fabricated assembly structure of h-WO_3 nanopillars may find various applications with the high capacitance achieved.

4. EXPERIMENTAL SECTION

4.1. Synthesis of the Assembly Structure of h-WO_3 Nanopillars. All of the chemicals were analytical grade and were used without further purification. In a typical synthesis, 10 mL of 0.3 M HCl was slowly added dropwise into the 10 mL solution containing 0.6 g of $Na_2WO_4{\cdot}2H_2O$. After stirring for several minutes, 0.6 g of NaCl was added into the solution. Subsequently, the resultant solution was transferred to the Teflon-lined stainless steel autoclave with a capacity of 45 mL. The autoclave was then sealed and hydrothermally treated at 180 °C for 12 h. After the autoclave cooled to room temperature naturally, the precipitates were collected by centrifugation (5000 rpm) and washed several times by deionized water to remove the possible impurities. The powders were collected after 80 °C drying overnight.

4.2. Characterization. The crystallographic characsteristics of the samples were investigated with powder XRD using a Bruker D2 Phaser diffractometer, which was equipped with Cu Kα radiation (λ = 1.54184 Å) and working at 10 mA and 30 kV, respectively. The morphologies were investigated by an environmental scanning electron microscope (FEI/Philips XL30) and a field-emission transmission electron microscope (JEOL-2001F). The specific surface areas were obtained from the N_2 adsorption/desorption isotherms measured at 77 K (NOVA e1000, Quantachrome).

4.3. Electrochemical Characterization. For preparation of the working electrodes, the as-synthesized powders were mixed with acetylene black and poly(tetrafluoroethylene) binder (8:1:1 weight ratio) in isopropyl alcohol. The mixture was coated on the stainless steel net current collector. The resulting electrodes were pressed and dried at 80 °C overnight.

The electrochemical performances of the h-WO_3 nanopillar electrode were investigated using a cell with a three-electrode configuration in an aqueous 0.5 M H_2SO_4 electrolyte. A stainless steel net and SCE were used as the counter and reference electrodes. CV, galvanostatic charge/discharge profiles, and EIS were carried out using a CHI760E electrochemical workstation. CV tests and galvanostatic charge/discharge profiles were performed in the potential range −0.5 to 0 V (vs SCE). The EIS data at room temperature were carried out at frequencies from 10 mHz to 100 kHz with a magnitude of 5 mV under different bias voltages (−0.4 to −0.1 V). The EIS data at different temperatures were conducted at the same range and magnitude of frequencies at open-circuit potential. The cycling performance was measured using the supercapacitor testing system (LAND CT2001A).

■ ASSOCIATED CONTENT

Ⓢ Supporting Information

Mechanism of growth of the assembly structure of h-WO_3 nanopillars, imaginary capacitance, voltage drop, power performance, nitrogen absorption and desorption, elaboration of the capacitive behavior, rate ability, SEM images, and EIS spectra at different temperatures. This material is available free of charge via the Internet at http://pubs.acs.org.

■ AUTHOR INFORMATION

Corresponding Author

*E-mail: cy.zhi@cityu.edu.hk.

Notes

The authors declare no competing financial interest.

■ ACKNOWLEDGMENTS

This research was supported by the Early Career Scheme of the Research Grants Council of Hong Kong SAR, China, under Project CityU9041977, the Science Technology and Innovation Committee of Shenzhen Municipality (Grant JCYJ20130401145617276), and a grant from the City University of Hong Kong.

■ REFERENCES

(1) Simon, P.; Gogotsi, Y. Materials for Electrochemical Capacitors. *Nat. Mater.* **2008**, *7*, 845−854.

(2) Miller, J. R.; Simon, P. Electrochemical Capacitors for Energy Management. *Science* **2008**, *321*, 651−652.

(3) Wang, X.; Tian, W.; Liu, D. Q.; Zhi, C. Y.; Bando, Y.; Golberg, D. Unusual Formation of Alpha-Fe_2O_3 Hexagonal Nanoplatelets in N-Doped Sandwiched Graphene Chamber for High-Performance Lithium-Ions Batteries. *Nano Energy* **2013**, *2*, 257−267.

(4) Sasidharan, M.; Gunawardhana, N.; Yoshio, M.; Nakashima, K. WO_3 Hollow Nanospheres for High-Lithium Storage Capacity and Good Cyclability. *Nano Energy* **2012**, *1*, 503−508.
(5) Huang, K.; Zhang, Q. Rechargeable Lithium Battery Based on a Single Hexagonal Tungsten Trioxide Nanowire. *Nano Energy* **2012**, *1*, 172−175.
(6) Guan, H.; Wang, X.; Li, H.; Zhi, C. Y.; Zhai, T.; Bando, Y.; Golberg, D. CoO Octahedral Nanocages for High-Performance Lithium Ion Batteries. *Chem. Commun.* **2012**, *48*, 4878−4880.
(7) Tian, Y. Y.; Cong, S.; Su, W. M.; Chen, H. Y.; Li, Q. W.; Geng, F. X.; Zhao, Z. G. Synergy of $W_{18}O_{49}$ and Polyaniline for Smart Supercapacitor Electrode Integrated with Energy Level Indicating Functionality. *Nano Lett.* **2014**, *14*, 2150−2156.
(8) Wang, X. B.; Zhang, Y. J.; Zhi, C. Y.; Wang, X.; Tang, D.; Xu, Y.; Weng, Q.; Jiang, X.; Mitome, M.; Golberg, D.; et al. Three-Dimensional Strutted Graphene Grown by Substrate-Free Sugar Blowing for High-Power-Density Supercapacitors. *Nat. Commun.* **2013**, *4*, 2905−2912.
(9) Liu, B.; Liu, B. Y.; Wang, Q. F.; Wang, X. F.; Xiang, Q.; Chen, D.; Shen, G. Z. New Energy Storage Option: Toward $ZnCo_2O_4$ Nanorods/Nickel Foam Architectures for High-Performance Supercapacitors. *ACS Appl. Mater. Interfaces* **2013**, *5*, 10011−10017.
(10) Liu, D. Q.; Wang, X.; Wang, X. B.; Tian, W.; Liu, J.; Zhi, C. Y.; He, D.; Bando, Y.; Golberg, D. Ultrathin Nanoporous Fe_3O_4−Carbon Nanosheets with Enhanced Supercapacitor Performance. *J. Mater. Chem. A* **2013**, *1*, 1952−1955.
(11) Xia, X. H.; Tu, J. P.; Wang, X. L.; Gu, C. D.; Zhao, X. B. Hierarchically porous NiO film grown by chemical bath deposition *via* a colloidal crystal template as an electrochemical pseudocapacitor material. *J. Mater. Chem.* **2011**, *21*, 671−679.
(12) Singh, A. K.; Sarkar, D.; Khan, G. G.; Mandal, K. Hydrogenated NiO nanoblock architecture for high performance pseudocapacitor. *ACS Appl. Mater. Interfaces* **2014**, *6*, 4684−4692.
(13) Wu, X.; Zeng, Y.; Gao, H. R.; Su, J.; Liu, J. P.; Zhu, Z. H. Template synthesis of hollow fusiform $RuO_2{\cdot}xH_2O$ nanostructure and its supercapacitor performance. *J. Mater. Chem. A* **2013**, *1*, 469−472.
(14) Yuan, G. Z.; Yang, L.; Hou, L. R.; Shen, L. F.; Zhang, X. G.; Lou, X. W. D. Growth of ultrathin mesoporous Co_3O_4 nanosheet arrays on Ni foam for high-performance electrochemical capacitors. *Energy Environ. Sci.* **2012**, *5*, 7883−7887.
(15) Meng, W. J.; Chen, W.; Zhao, L.; Huang, Y.; Zhu, M. S.; Huang, Y.; Fu, Y. Q.; Geng, F. X.; Yu, J.; Chen, X. F.; Zhi, C. Y. Porous Fe_3O_4/carbon composite electrode material prepared from metal−organic framework template and effect of temperature on its capacitance. *Nano Energy* **2014**, *8*, 133−140.
(16) Conway, B. E. *Electrochemical Supercapacitors*; Kluwer Academic/Plenum Publishers: New York, 1999.
(17) Tao, J. Y.; Liu, N. S.; Li, L. Y.; Gao, Y. H. Hierarchical Nanostructures of Polypyrrole@MnO_2 Composite Electrodes for High Performance Solid-State Asymmetric Supercapacitors. *Nanoscale* **2014**, *6*, 2922−2928.
(18) Wang, X. F.; Liu, B.; Liu, R.; Wang, Q. F.; Hou, X. J.; Chen, D.; Wang, R. M.; Shen, G. Z. Fiber-Based Flexible All-Solid-State Asymmetric Supercapacitors for Integrated Photodetecting System. *Angew. Chem., Int. Ed.* **2014**, *53*, 1849−1853.
(19) Xu, J.; Wang, Q. F.; Wang, X. W.; Xiang, Q.; Hang, B.; Chen, D.; Shen, G. Z. Flexible Asymmetric Supercapacitors Based Upon Co_9S_8 Nanorod/Co_3O_4@RuO_2 Nanosheet Arrays on Carbon Cloth. *ACS Nano* **2013**, *7*, 5453−5462.
(20) Liu, N. S.; Ma, W. Z.; Tao, J. Y.; Zhang, X. H.; Su, J.; Li, L. Y.; Yang, C. X.; Gao, Y. H.; Golberg, D.; Bando, Y. Cable-Type Supercapacitors of Three-Dimensional Cotton Thread Based Multi-Grade Nanostructures for Wearable Energy Storage. *Adv. Mater.* **2013**, *25*, 4925−4931.
(21) Tao, J. Y.; Liu, N. S.; Ma, W. Z.; Ding, L.; Li, L. Y.; Su, J.; Gao, Y. H. Solid-State High Performance Flexible Supercapacitors Based on Polypyrrole−MnO_2−Carbon Fiber Hybrid Structure. *Sci. Rep.* **2013**, *3*, 2286−2292.
(22) Feng, J.; Sun, X.; Wu, C. Z.; Peng, L. L.; Lin, C. W.; Hu, S. L.; Yang, J. L.; Xie, Y. Metallic few-layered VS_2 ultrathin nanosheets: high two-dimensional conductivity for in-plane supercapacitors. *J. Am. Chen. Soc.* **2011**, *133*, 17832−17838.
(23) Zhang, C. L.; Yin, H. H.; Han, M.; Dai, Z. H.; Pang, H.; Zheng, Y. L.; Lan, Y. Q.; Bao, J. C.; Zhu, J. M. Two-dimensional tin selenide nanostructures for flexible all-solid-state supercapacitors. *ACS Nano* **2014**, *8*, 3761−3770.
(24) Wang, Q. F.; Xu, J.; Wang, X. F.; Liu, B.; Hou, X. J.; Yu, G.; Wang, P.; Chen, D.; Shen, G. Z. Core−shell $CuCo_2O_4$@MnO_2 nanowires on carbon fabrics as high-performance materials for flexible, all-solid-state, electrochemical capacitors. *ChemElectroChem* **2014**, *1*, 559−564.
(25) Xu, J.; Wang, Q. F.; Wang, X. W.; Xiang, Q. Y.; Liang, Bo.; Chen, Di.; Shen, G. Z. Flexible asymmetric supercapacitors based upon Co_9S_8 nanorod/Co_3O_4@RuO_2 nanosheet arrays on carbon cloth. *ACS Nano* **2013**, *7*, 5453−5462.
(26) Chen, P. C.; Shen, G. Z.; Sukcharoenchoke, S.; Zhou, C. W. Flexible and transparent supercapacitor based on In_2O_3 nanowire/carbon nanotube heterogeneous films. *Appl. Phys. Lett.* **2009**, *94*, 043313.
(27) Wang, X. F.; Liu, B.; Xiang, Q. Y.; Wang, Q. F.; Hou, X. J.; Chen, D.; Shen, G. Z. Spray-painted binder-free SnSe electrodes for high-performance energy-storage devices. *ChemSusChem* **2014**, *7*, 308−313.
(28) Augustyn, V.; Come, J.; Lowe, M. A.; Kim, J. W.; Taberna, P. L.; Tolbert, S. H.; Abruña, H. D.; Simon, P.; Dunn, B. High-Rate Electrochemical Energy Storage through Li^+ Intercalation Pseudocapacitance. *Nat. Mater.* **2013**, *12*, 518−522.
(29) Chang, K. H.; Hu, C. C.; Huang, C. M.; Liu, Y. L.; Chang, C. I. Microwave-Assisted Hydrothermal Synthesis of Crystalline WO_3−$WO_3{\cdot}0.5H_2O$ Mixtures for Pseudocapacitors of the Asymmetric Type. *J. Power Sources* **2011**, *196*, 2387−2392.
(30) Huang, C. C.; Xing, W.; Zhuo, S. P. Capacitive Performances of Amorphous Tungsten Oxide Prepared by Microwave Irradiation. *Scr. Mater.* **2009**, *61*, 985−987.
(31) Park, S. H.; Kim, Y. H.; Lee, T. G.; Shon, H. K.; Park, H. M.; Song, J. Y. Synthesis and Electrochemical Capacitance of Long Tungsten Oxide Nanorod Arrays Grown Vertically on Substrate. *Mater. Res. Bull.* **2012**, *47*, 3612−3618.
(32) Jo, C.; Hwang, I.; Lee, J.; Lee, C. W.; Yoon, S. Investigation of Pseudocapacitive Charge-Storage Behavior in Highly Conductive Ordered Mesoporous Tungsten Oxide Electrodes. *J. Phys. Chem. C* **2011**, *115*, 11880−11886.
(33) Xiao, W.; Liu, W.; Mao, X.; Zhu, H.; Wang, D. Na_2SO_4-Assisted Synthesis of Hexagonal-Phase WO_3 Nanosheet Assemblies with Applicable Electrochromic and Adsorption Properties. *J. Mater. Chem. A* **2013**, *1*, 1261−1269.
(34) Jo, C.; Hwang, J.; Song, H.; Dao, A. H.; Kim, Y. T.; Lee, S. H.; Hong, S. W.; Yoon, S.; Lee, J. Block-Copolymer-Assisted One-Pot Synthesis of Ordered Mesoporous WO_{3-x}/Carbon Nanocomposites as High-Rate-Performance Electrodes for Pseudocapacitors. *Adv. Funct. Mater.* **2013**, *23*, 3747−3754.
(35) Zheng, H.; Ou, J. Z.; Strano, M. S.; Kaner, R. B.; Mitchell, A.; Kalantar zadeh, K. Nanostructured Tungsten Oxide—Properties, Synthesis, and Applications. *Adv. Funct. Mater.* **2011**, *21*, 2175−2196.
(36) Gerand, B.; Nowogrocki, G.; Figlarz, M. A New Tungsten Trioxide Hydrate, $WO_3{\cdot}1/3H_2O$—Preparation, Characterization, and Crystallographic Study. *J. Solid State Chem.* **1981**, *38*, 312−320.
(37) Figlarz, M. New Oxides in the WO_3−MoO_3 System. *Prog. Solid State Chem.* **1989**, *19*, 1−46.
(38) Seguin, L.; Figlarz, M.; Pannetier, J. A Novel Supermetastable WO_3 Phase. *Solid State Ionics* **1993**, *63*−*5*, 437−441.
(39) Pfeifer, J.; Guifang, C.; Tekula-Buxbaum, P.; Kiss, B. A. A Reinvestigation of the Preparation of Tungsten Oxide Hydrate $WO_3{\cdot}1/3H_2O$. *J. Solid State Chem.* **1995**, *119*, 90−97.
(40) Guo, J. Open Structure Tungstates: Synthesis, Reactivity and Ionic Mobility. *Solid State Ionics* **1992**, *53*−*56*, 305−314.

(41) Masarapu, C.; Zeng, H. F.; Hung, K. H.; Wei, B. Effect of Temperature on the Capacitance of Carbon Nanotube Supercapacitors. *ACS Nano* **2009**, *3*, 2199−2206.
(42) Liu, P.; Verbrugge, M.; Soukiazian, S. Influence of Temperature and Electrolyte on the Performance of Activated-Carbon Supercapacitors. *J. Power Sources* **2006**, *156*, 712−718.
(43) Tsai, W. Y.; Lin, R.; Murali, S.; Li Zhang, L.; McDonough, J. K.; Ruoff, R. S.; Taberna, P. L.; Gogotsi, Y.; Simon, P. Outstanding Performance of Activated Graphene Based Supercapacitors in Ionic Liquid Electrolyte from −50 to 80 °C. *Nano Energy* **2013**, *2*, 403−411.
(44) Li, W. Y.; Xu, K. B.; Lei, A.; Jiang, F. R.; Zhou, X. Y.; Yang, J. M.; Chen, Z. G.; Zou, R. J.; Hu, J. Q. Effect of Temperature on the Performance of Ultrafine MnO_2 Nanobelt Supercapacitors. *J. Mater. Chem. A* **2014**, *2*, 1443−1447.
(45) Wang, J. G.; Yang, Y.; Huang, Z. H.; Kang, F. Effect of Temperature on the Pseudo-Capacitive Behavior of Freestanding MnO_2@Carbon Nanofibers Composites Electrodes in Mild Electrolyte. *J. Power Sources* **2013**, *224*, 86−92.
(46) Wang, J. G.; Yang, Y.; Huang, Z. H.; Kang, F. Synthesis and Electrochemical Performance of MnO_2/CNTs-Embedded Carbon Nanofibers Nanocomposites for Supercapacitors. *Electrochim. Acta* **2012**, *75*, 213−219.
(47) Yan, J.; Khoo, E.; Sumboja, A.; Lee, P. S. Facile Coating of Manganese Oxide on Tin Oxide Nanowires with High-Performance Capacitive Behavior. *ACS Nano* **2010**, *4*, 4247−4255.
(48) Salmaoui, S.; Sediri, F.; Gharbi, N.; Perruchot, C.; Jouini, M. Hexagonal Hydrated Tungsten Oxide Nanomaterials: Hydrothermal Synthesis and Electrochemical Properties. *Electrochim. Acta* **2013**, *108*, 634−643.
(49) Michailovski, A.; Kiebach, R.; Bensch, W.; Grunwaldt, J. D.; Baiker, A.; Komarneni, S.; Patzke, G. R. Morphological and Kinetic Studies on Hexagonal Tungstates. *Chem. Mater.* **2007**, *19*, 185−197.
(50) Komaba, S.; Kumagai, N.; Kato, K.; Yashiro, H. Hydrothermal Synthesis of Hexagonal Tungsten Trioxide From Li_2WO_4 Solution and Electrochemical Lithium Intercalation Into the Oxide. *Solid State Ionics* **2000**, *135*, 193−197.
(51) Kumagai, N.; Umetzu, Y.; Tanno, K.; Pereira Ramos, J. P. Synthesis of Hexagonal Form of Tungsten Trioxide and Electrochemical Lithium Insertion Into the Trioxide. *Solid State Ionics* **1996**, *86*−*8*, 1443−1449.
(52) Shibuya, M.; Miyauchi, M. Site-Selective Deposition of Metal Nanoparticles on Aligned WO_3·Nanotrees for Super-Hydrophilic Thin Films. *Adv. Mater.* **2009**, *21*, 1373−1376.
(53) Gu, Z.; Zhai, T.; Gao, B.; Sheng, X.; Wang, Y.; Fu, H.; Ma, Y.; Yao, J. Controllable Assembly of WO_3 Nanorods/Nanowires Into Hierarchical Nanostructures. *J. Phys. Chem. B* **2006**, *110*, 23829−23836.
(54) Baeck, S. H.; Jaramillo, T.; Stucky, G. D.; McFarland, E. W. Controlled Electrodeposition of Nanoparticulate Tungsten Oxide. *Nano Lett.* **2002**, *2*, 831−834.
(55) Wang, J.; Khoo, E.; Lee, P. S.; Ma, J. Synthesis, Assembly, and Electrochromic Properties of Uniform Crystalline WO_3 Nanorods. *J. Phys. Chem. C* **2008**, *112*, 14306−14312.
(56) Wang, J.; Khoo, E.; Lee, P. S.; Ma, J. Controlled Synthesis of WO_3 Nanorods and Their Electrochromic Properties in H_2SO_4 Electrolyte. *J. Phys. Chem. C* **2009**, *113*, 9655−9658.
(57) Solbrand, A.; Rensmo, H.; Hjelm, J. Li^+ Ion Insertion in TiO_2 (Anatase). 2. Voltammetry on Nanoporous Films. *J. Phys. Chem. B* **1997**, *101*, 7717−7722.
(58) Ardizzone, S.; Fregonara, G.; Trasatti, S. Inner and Outer Active Surface of RuO_2 Electrodes. *Electrochim. Acta* **1990**, *35*, 263−267.
(59) Baronetto, D.; Krstajic, N.; Trasatti, S. Reply To "Note On A Method To Interrelate Inner And Outer Electrode Areas" By H. Vogt. *Electrochim. Acta* **1994**, *39*, 2359−2362.